

Investigation of the light field of a semiconductor diode laser

A. V. Ankudinov,^{1,2,*} M. L. Yanul,³ S. O. Slipchenko,¹ A. V. Shelaev,³ P. S. Dorozhkin,³
A. A. Podoskin,¹ and I. S. Tarasov¹

¹*Ioffe Physical-Technical Institute of the Russian Academy of Sciences, 26 Polytekhnicheskaya, Saint Petersburg, 194021, Russia*

²*St. Petersburg National Research University of Information Technology, Mechanics & Optics, 49 Kronverkskiy, Saint Petersburg, 197101, Russia*

³*NT-MDT Co., Building 100, Zelenograd, Moscow, 124482, Russia*
**alexander.ankudinov@mail.ioffe.ru*

Abstract: Scanning near-field optical microscopy was applied to study, with sub-wavelength spatial resolution, the near- and the far-field distributions of propagating modes from a high-power laser diode. Simple modeling was also performed and compared with experimental results. The simulated distributions were consistent with the experiment and permitted clarification of the configuration of the transverse modes of the laser.

©2014 Optical Society of America

OCIS codes: (140.5960) Semiconductor lasers; (030.4070) Modes; (180.4243) Near-field microscopy; (100.3008) Image recognition, algorithms and filters.

References and links

1. A. Al-Muhanna, L. J. Mawst, D. Botez, D. Z. Garbuzov, R. U. Martinelli, and J. C. Conolly, "High-power (>10 W) continuous-wave operation from 100- μm -aperture 0.97- μm -emitting Al-free diode lasers," *Appl. Phys. Lett.* **73**(9), 1182–1184 (1998).
2. J. K. Wade, L. J. Mawst, D. Botez, and J. A. Morris, "8.8 W CW power from broad-waveguide Al-free active-region ($\lambda = 805\text{nm}$) diode lasers," *Electron. Lett.* **34**(11), 1100 (1998).
3. N. A. Pikhtin, S. O. Slipchenko, Z. N. Sokolova, A. L. Stankevich, D. A. Vinokurov, I. S. Tarasov, and Zh. I. Alferov, "16W continuous-wave output power from 100 μm -aperture laser with quantum well asymmetric heterostructure," *Electron. Lett.* **40**(22), 1413–1414 (2004).
4. P. Crump, G. Blume, K. Paschke, R. Staske, A. Pietrzak, U. Zeimer, S. Einfeldt, A. Ginolas, F. Bugge, K. Häusler, P. Ressel, H. Wenzel, and G. Erbert, "20 W continuous wave reliable operation of 980 nm broad-area single emitter diode lasers with an aperture of 96 μm ," *Proc. SPIE* **7198**, 719814 (2009).
5. I. B. Petrescu-Prahova, P. Modak, E. Goutain, D. Silan, D. Bambrick, J. Riordan, T. Moritz, S. D. McDougall, B. Qiu, and J. H. Marsh, "High d/gamma values in diode laser structures for very high power," *Proc. SPIE* **7198**, 71981I (2009).
6. I. B. Petrescu-Prahova, M. Buda, and T. G. van de Roer, "Design of a 1W, single filament laser diode," *IEICE Trans. Electron.* **E77-C**, 1472–1479 (1994).
7. S. O. Slipchenko, N. A. Pikhtin, N. V. Fetisova, M. A. Khomylev, A. A. Marmalyuk, D. B. Nikitin, A. A. Padalitsa, P. V. Bulaev, I. D. Zalevskii, and I. S. Tarasov, "Laser diodes ($\lambda=0.98 \mu\text{m}$) with a narrow radiation pattern and low internal optical losses," *Tech. Phys. Lett.* **29**(12), 980–983 (2003).
8. S. O. Slipchenko, D. A. Vinokurov, N. A. Pikhtin, Z. N. Sokolova, A. L. Stankevich, I. S. Tarasov, and Zh. I. Alferov, "Ultralow internal optical loss in separate-confinement quantum-well laser heterostructures," *Semiconductors* **38**(12), 1430–1439 (2004).
9. P. Crump, A. Pietrzak, F. Bugge, H. Wenzel, G. Erbert, and G. Tränkle, "975 nm high power diode lasers with high efficiency and narrow vertical far field enabled by low index quantum barriers," *Appl. Phys. Lett.* **96**(13), 131110 (2010).
10. V. Ya. Aleshkin, A. A. Afonenko, and N. B. Zvonkov, "Difference mode generation in injection lasers," *Semiconductors* **35**(10), 1203–1207 (2001).
11. B. N. Zvonkov, A. A. Biryukov, A. V. Ershov, S. M. Nekorkin, V. Ya. Aleshkin, V. I. Gavrilenko, A. A. Dubinov, K. V. Maremyanin, S. V. Morozov, A. A. Belyanin, V. V. Kocharovskiy, and V. V. Kocharovskiy, "Room-temperature intracavity difference-frequency generation in butt-joint diode lasers," *Appl. Phys. Lett.* **92**(2), 021122 (2008).
12. D. A. Vinokurov, A. L. Stankevich, V. V. Shamakhov, V. A. Kapitonov, A. Y. Leshko, A. V. Lyutetskii, D. N. Nikolaev, N. A. Pikhtin, N. A. Rudova, Z. N. Sokolova, S. O. Slipchenko, M. A. Khomylev, and I. S. Tarasov, "High-power lasers ($\lambda= 940\text{--}980 \text{ nm}$) based on asymmetric GaInAs/GaInAsP/AlGaAs separate-confinement heterostructure," *Semiconductors* **40**(6), 745–748 (2006).

13. S. O. Slipchenko, A. D. Bondarev, D. A. Vinokurov, D. N. Nikolaev, N. V. Fetisova, Z. N. Sokolova, N. A. Pikhin, and I. S. Tarasov, "Selection of modes in transverse-mode waveguides for semiconductor lasers based on asymmetric heterostructures," *Semiconductors* **43**(1), 112–116 (2009).
14. S. A. Akhmanov and S. Yu. Nikitin, *Physical Optics* (Oxford, 1997).
15. H. C. Casey, Jr. and M. B. Panish, *Heterostructure Lasers. Part A. Fundamental Principles* (New York, 1978).
16. R. H. Webb, "Confocal optical microscopy," *Rep. Prog. Phys.* **59**(3), 427–471 (1996).
17. B. Hecht, B. Sick, U. P. Wild, V. Deckert, R. Zenobi, O. J. F. Martin, and D. W. Pohl, "Scanning near-field optical microscopy with aperture probes: fundamentals and applications," *J. Chem. Phys.* **112**(18), 7761–7774 (2000).
18. D. K. Young, M. P. Mack, A. C. Abare, M. Hansen, L. A. Coldren, S. P. Denbaars, E. L. Hu, and D. D. Awschalom, "Near-field scanning optical microscopy of indium gallium nitride multiple-quantum-well laser diodes," *Appl. Phys. Lett.* **74**(16), 2349–2351 (1999).
19. P.-A. Lemoine, V. Moreau, M. Bahriz, Y. De Wilde, R. Colombelli, L. R. Wilson, and A. B. Krysa, "Intracavity near-field optical imaging of a mid-infrared quantum cascade laser mode," *Mater. Sci. Eng. B* **149**(3), 270–274 (2008).
20. <http://www.ntmdt.com/device/ntegra-spectra>.
21. M. Abramowitz and I. A. Stegun, *Handbook of Mathematical Functions* (New York, 1964).
22. A. V. Ankudinov, V. P. Evtikhiev, E. Yu. Kotelnikov, A. N. Titkov, and R. Laiho, "Voltage distributions and nonoptical catastrophic mirror degradation in high power InGaAs/AlGaAs/GaAs lasers studied by Kelvin probe force microscopy," *J. Appl. Phys.* **93**(1), 432–437 (2003).
23. A. V. Ankudinov, V. P. Evtikhiev, K. S. Ladutenko, M. G. Rastegaeva, A. N. Titkov, and R. Laiho, "Kelvin probe force and surface photovoltage microscopy observation of minority holes leaked from active region of working InGaAs/AlGaAs/GaAs laser diode," *J. Appl. Phys.* **101**(2), 024504 (2007).

1. Introduction

Modern semiconductor lasers are widely used in various fields of science and technology. In continuous operation, the radiation power from 100 μm -aperture laser diode can exceed 10 W [1–5], which corresponds to a radiation density at the emitting facet of about 10^{11} W/m^2 (several hundred times greater than at the Sun's surface). To manufacture such high-power emitters, the heterostructures with a so-called broadened waveguide are used [6–9]. With increasing thickness of the waveguide, not only a fundamental transverse mode of the 0th order arises, but also additional modes of higher orders may survive. Most optical applications exploit only the fundamental mode. However, a number of practical applications, for example, mixing two laser frequencies from different active regions to produce far-infrared radiation [10,11], require saving certain higher-order transverse modes. As was proposed and experimentally demonstrated in [12], it is possible to select specific transverse modes by choosing the position of the active region in the waveguide.

Figure 1 presents characteristics and the design of the high-power semiconductor laser diode emitting at 1.07 μm wavelengths. The laser heterostructure consists of wide-band emitters $\text{Al}_{0.25}\text{Ga}_{0.75}\text{As}$, a 1.9 μm thick GaAs waveguide, and an active area of an 8 nm thick InGaAs quantum well (qw), that is shifted from the waveguide center towards the p-emitter by 0.75 μm . The numerical solution of the wave equation for this heterostructure using the approximation of a dielectric waveguide (neglecting the light absorption by charge carriers and amplification) gives three stationary modal configurations of the electromagnetic field [13]. Figure 1(b) shows profiles of the allowed TE modes (TE denotes transverse electric field that is perpendicular to the direction of the light propagation and lies in the plane of the qw).

Simultaneous fulfillment of threshold conditions for the generation of all three modes is unlikely. However, if we analyze the factors determining the threshold conditions for the 1st and the 2nd modes, we see the following. The right minimum of the 2nd mode is located at the same place as the qw (see the band diagram in Fig. 1(c)), i.e. the qw is effectively overlapped by the electric field. This allows maximally amplifying the radiation in the active region, i.e. it creates the most favorable conditions for exciting the 2nd mode compared to other modes. The same wavelength may be simultaneously excited by another, the 1st mode that also has a right maximum close to the qw. In this case, the amplification decrease in the active region must be compensated by decreasing optical losses in the emitter layers. The

calculations show, for an equal redistribution of the power between the two modes and average internal optical losses of 1.5 cm^{-1} , the critical optical cavity length, which simultaneously provides lasing threshold conditions, is $2180 \mu\text{m}$. This value is close to the optical cavity lengths in the laser samples chosen for our experiments.

In contrast to the 0th mode, the modes of higher order are much weaker localized within the waveguide. The calculations show the optical confinement factor for the emitter layers increases from 0.53% for the 0th mode to 2.3% and 6.2% for the 1st and 2nd modes, respectively. It explains higher internal optical losses in the selected laser samples, compared with 0.34 cm^{-1} in similar structures [3] when the threshold conditions have been only fulfilled for the fundamental 0th mode.

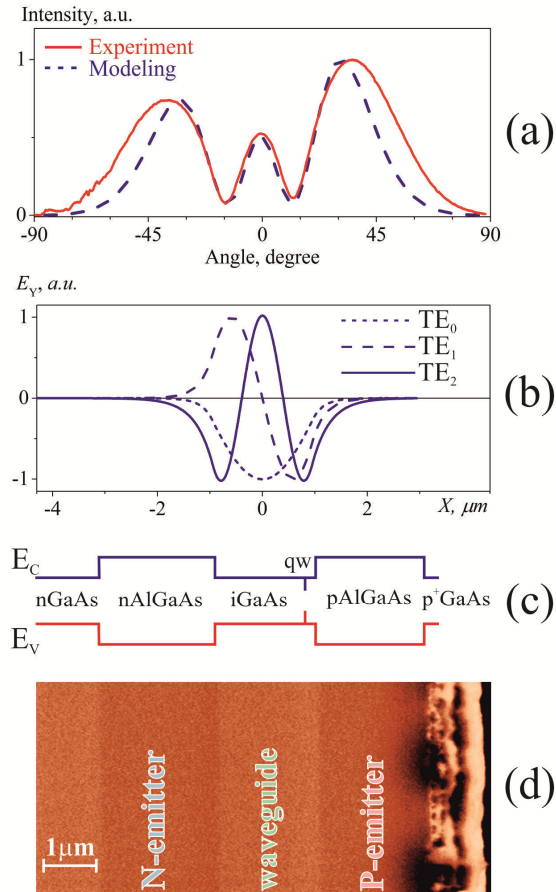


Fig. 1. Characteristics and the design of the laser diode. An experimental far-field laser radiation pattern (red solid line) and modeled divergence (blue dashed line) calculated for a linear combination of the 2nd the 1st TE modes with the amplitude ratio of the electric fields 0.267 and the phase difference of 16° , (a). Electric field profiles of three TE modes corresponding to the possible solutions of the wave equation for the laser heterostructure, (b). Energy band schematics for the laser heterostructure, (c). Scanning electron microscopy image of the laser facet identifies main layers of the heterostructure, (d). The far-field laser radiation pattern was measured in the pulsed operation regime with parameters: pulse duration $5 \mu\text{s}$, repetition frequency 1 kHz , current amplitude 2 A (threshold current 0.35 A), optical power per emitting facet 0.6 W .

The far-field laser radiation pattern measured in the plane perpendicular to the p-n junction of the laser is shown in Fig. 1(a). It has an asymmetric shape that cannot arise from

mixing the symmetric 0th mode with the main 2nd mode. However it can be associated with the simultaneous excitation of the asymmetric 1st mode. Shown in the same figure, the calculated far-field laser radiation pattern was obtained by integrating [14,15] the electric field resulting from a linear combination of the 2nd and the 1st TE modes. An agreement of theory and experiment was reached under fourfold amplitude ratio of the electric fields of these modes and a phase difference of 16° . However, there are other possible combinations of these modes that satisfactorily describe the experiment as well. More accurate and unambiguous information on the mode configuration can be extracted from the near-field radiation distributions measured directly on the surface of the emitting facet of the laser. To this end, the methods of scanning confocal microscopy [16] and scanning near-field optical microscopy (SNOM) [17] were applied in our work. The semiconductor lasers were investigated by SNOM, e.g. in [18,19]. However, as far as we know, SNOM was not previously applied to clarify the transverse mode configuration.

2. Methods and results

Distributions of the radiative emissions from the above-described laser were investigated under ambient conditions using the scanning probe optical nanolaboratory Ntegra Spectra (NT-MDT, Russia) [20]. Figure 2 presents simplified diagrams for measurements in scanning confocal microscopy and SNOM regimes. In both cases, the emitting facet, the natural cleavage of the laser heterostructure, is almost parallel to the focal plane of the lens. To minimize the thermal drift for stabilizing the laser spectrum and the radiation pattern, the laser diode was pumped by a pulsed current source. In the confocal regime of measurements, we used lenses with numerical aperture $NA = 0.9, 0.7,$ and 0.5 . In the SNOM regime, we used cantilevers with a metal coated pyramidal SiO_2 probe and an aperture created on the probe end by the focused ion beam process. Such cantilevers may be also simultaneously used for surface topography imaging by standard atomic force microscopy (AFM) techniques. The aperture diameter was about 100 nm ; the radiation penetrating through the nanoaperture was collected by a lens with $NA = 0.5$.

The Ntegra Spectra instrument allows measuring and recording distribution of full laser emission spectrum in all three directions (X,Y,Z) – both in confocal and in SNOM configurations. Post-processing of the recorded data allowed exploring variations in the intensity of any selected part of the laser spectrum both along a horizontal XY plane of the emitting facet (the near-field) or along vertical XZ and YZ planes (a transition from the near-field to the far-field). In the SNOM regime, the Z values are always positive, since the probe physically cannot penetrate into the surface. In the confocal regime, the Z values can be of any sign, because the focus of the lens is adjusted, both above and below the surface.

Shown in Fig. 3, the lasing spectrum for the laser diode measured in the confocal regime. Almost all the radiation is concentrated in the spectral range of 1073-1075 nm, within which 8 lines can be separated. The lines in the spectrum do not originate from the different transverse modes, but occur from different longitudinal modes [15]. In this case the characteristic distance between the lines is: $\Delta\lambda/\lambda = \lambda/2L(n - \lambda \times dn/d\lambda)$, where the cavity length L , the mean lasing wavelength λ , and the refractive index n of the waveguide material are used. Given the parameters of the laser structure, this distance is calculated to be a few angstroms, which is consistent with the shape of the measured spectrum.

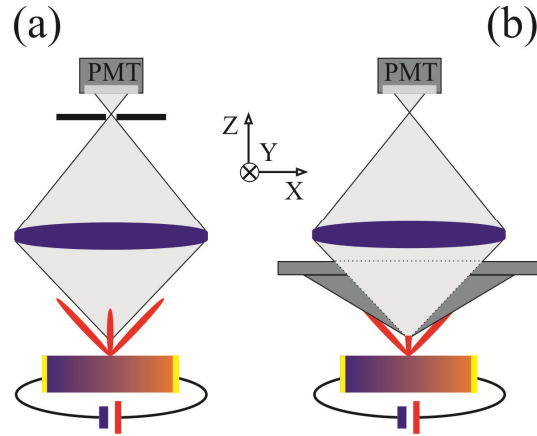


Fig. 2. Experimental schemes to study laser radiation distributions in confocal (a) and SNOM (b) measurement regimes. To activate the laser, a pulsed power supply was used: current pulse duration $5 \mu s$, repetition frequency $1 kHz$, current pulse amplitude $2 A$. In the Cartesian coordinates of the triple of vectors X, Y and Z is selected according to the generally accepted description for semiconductor lasers [15]: X vector points along the normal to the plane of the heterostructure layers; Y vector is in the plane of the heterostructure layers; Z vector is normal to the emitting facet.

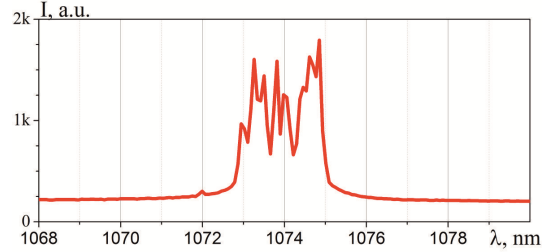


Fig. 3. A lasing spectrum of the high-power laser diode, as measured on the emitting facet by scanning confocal optical microscopy.

Figure 4(a) shows a simulated image in the XZ plane, corresponding to the light distribution radiated by the 2nd TE mode in the vicinity of the emitting facet. The 2D wave equation, with one point source at the origin, has a solution in the form of the Hankel function, which behaves far from the source like a damped sine wave, $\sin(\omega t - kr)/\sqrt{r}$ [21]. Model brightness signal, $S(r)$, was calculated as the time-averaged intensity of the interference, $I(r, t)$, of such damped waves from three sources:

$$I(r, t) = \left(\frac{A_l \sin(\omega t - k|r - r_l|)}{\sqrt{|r - r_l|}} + \frac{A_c \sin(\omega t - k|r - r_c|)}{\sqrt{|r - r_c|}} + \frac{A_r \sin(\omega t - k|r - r_r|)}{\sqrt{|r - r_r|}} \right)^2 \quad (1a)$$

$$\begin{aligned}
S(r) = \langle I(r, t) \rangle = & \frac{A_L^2}{2|r-r_L|} + \frac{A_C^2}{2|r-r_C|} + \frac{A_R^2}{2|r-r_R|} \\
& + \frac{A_L A_C \cos[k(|r-r_L| - |r-r_C|)]}{\sqrt{|r-r_L| \times |r-r_C|}} \\
& + \frac{A_L A_R \cos[k(|r-r_L| - |r-r_R|)]}{\sqrt{|r-r_L| \times |r-r_R|}} \\
& + \frac{A_C A_R \cos[k(|r-r_C| - |r-r_R|)]}{\sqrt{|r-r_C| \times |r-r_R|}}
\end{aligned} \tag{1b}$$

Wave-number $k = 2\pi/1.07 \mu\text{m}^{-1}$; central (C), with the coordinate r_C , left (L), r_L , and right (R), r_R , sources were separated from each other by the distance of $3\lambda/4$, in accordance with the intervals between extremes of the simulated electric field profile of the 2nd mode, see Fig. 1(b). To simulate the light distribution for the 2nd mode, see the model image in Fig. 4(a), the following amplitudes are used: $A_C = 1, A_L = A_R = -1$. Equation (1b) also permits to qualitatively simulate the radiation resulting from the 0th mode ($A_C = 1, A_L = A_R = 0$), from the 1st mode ($A_C = 0, A_L = -A_R = 1$), as well as from an arbitrary linear combination of all three modes. In general, the A_C, A_L and A_R are complex numbers.

For the sake of simplicity, the modeling only exploits three point sources and neglects the small mismatch between the extrema positions in the electric field distributions for the 1st and the 2nd modes. Although the modeling is therefore limited in accuracy, it allows describing the light fields for all possible combinations of the modes. Note that, according to Eq. (1b), near the sources, the signals ($S_{L,C,R} := S|_{r=r_{L,C,R} + \varepsilon}$, where ε is infinitely small constant) obey proportions: $S_L : S_C : S_R = |A_L^2| : |A_C^2| : |A_R^2|$. This relation will be used when analyzing the experimental SNOM signal.

The waveguide thickness $d \approx 2\lambda$ determines the typical width of the laser near-field. It is of the order of λ , and in this case, according to the basics of diffraction [14], the characteristic far-field features must be already formed at the distance just several wavelengths above the facet ($\sim d^2/\lambda \approx 4\lambda$). This is exactly what is observed in the model image in Fig. 4(a), as well as in the experimental image in Fig. 4(b), obtained with the maximum numerical aperture lens $NA = 0.9$. At the top of the image, two side lobes are noticeably brighter than the central lobe, which, to a first approximation, is to be expected for the light divergence in the far-field, see Fig. 1(a). On the emitting facet, the SNOM signal is equally distributed between three maxima located every $0.8 \mu\text{m}$. This coincides with the distance $3\lambda/4$ between the point sources in the model.

In Fig. 4, the experimental images differ from the model image. This is due to the instrumental contributions, growing with decreasing NA of the lens. Already for $NA = 0.7$, see Fig. 4(c), the measured far-field is distorted: side lobes are observed propagating under more acute angles and are accompanied by satellites. In the image in Fig. 4(d), $NA = 0.5$ lens, the central lobe remains the brightest far from the emitting facet. Besides, on the emitting facet, the measured signal is presented by the multiple (7 or even more) peaks of different heights. The lenses with $NA = 0.9, 0.7$, and 0.5 , accept the light in the following angle ranges: $\pm 64^\circ$, $\pm 45^\circ$ and $\pm 30^\circ$. By integrating the experimental far-field profile in Fig. 1(a), it can be shown that the highest NA lens may detect almost all the light from the studied laser, about 93%; the lower NA lenses can collect, respectively, 67 and 34% of the light. Thus, the distortion's origin is that the lens loses an essential portion of the light from the side lobes. However, it is also appropriate to consider the data in terms of insufficient spatial resolution.

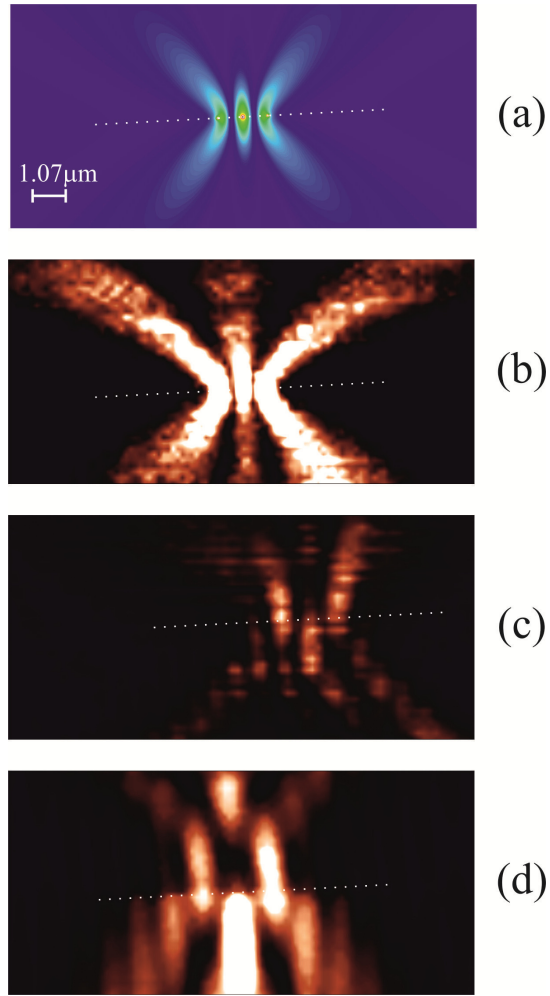


Fig. 4. Scanning confocal optical microscopy of the radiation distribution near the emitting facet of the operating laser diode. 2nd TE mode XZ image calculated by expression (1) (a). XZ signal distribution of the laser radiation (integrated intensity of spectrum in the 1074-1075 nm range), measured by the lenses $NA = 0.9$, (b), $NA = 0.7$, (c), and $NA = 0.5$, (d). Dotted lines in the images indicate the emitting facet position (laser layers are below the line). All images have the same scale and were taken from nearly the same sample area.

In scanning confocal optical microscopy, the optimal resolution is achieved when laser illumination is focused into a spot (“point”), limited by the diffraction at the lens aperture, and, through the same lens, the registration pinhole is projected into the same spot [16]. In this case, according to the theory [16], the air lens with $NA = 0.9$ has an axial resolution no better than 2λ : $\Delta z_{NA=0.9} = 1.5 \times \lambda / NA^2 = 1.5 \times 1.07 / 0.81 \approx 2 \mu m$. The confocal planar resolution ($\Delta x = 0.4 \times \lambda / NA$) of this lens is approximately a half of λ : $\Delta x_{NA=0.9} \approx 0.44 \lambda \approx 0.5 \mu m$. However, the semiconductor laser is not a true “point” light source. The light sources are distributed over a strip that is about $100 \mu m$ long and has a width defined by the dimensions of the TE mode. Therefore, regardless the confocal regime was applied, the planar resolution of the image in Fig. 4(b) is hardly better than Rayleigh criterion: $\Delta x_{NA=0.9} \approx 0.68 \times \lambda / NA \approx 0.68 \lambda \approx 0.73 \mu m$.

In the near-field, see Fig. 4(b) at the emitting facet, three peaks of almost equal height are detected. To reveal the local mode configuration responsible for the measured picture, we need first to find out how reliable this equality is - considering it was measured in a

diffraction limited confocal regime by a high NA lens. The distance between the peaks, $0.8 \mu\text{m}$, is close to the planar resolution. This seems to be sufficient to qualitatively visualize the expected near-field response with three maxima. (The images in Figs. 4(c) and 4(d), obtained with a planar resolution of $0.93 \mu\text{m}$ and, respectively, $1.31 \mu\text{m}$, do not agree even qualitatively with the expected emission pattern.) However, this is not sufficient for accurate quantitative analysis. In particular, the measured amplitude of the side peaks contains the contribution from the central maximum of the expected near-field, and in the central peak there is the contribution from the side maxima. It is a well-known instrumental effect: the output signal is the convolution of the input signal with the instrumental response function of the device. If, for example, the expected near-field were represented by three equal maxima, in the measured near-field the central peak should be above the side peaks, due to the instrumental effect of the $NA = 0.9$ lens.

Significant resolution improvement is provided by the SNOM with aperture cantilevers. The SNOM image of the radiation intensity distribution at the laser facet (XY plane) and the contact AFM topography image, Figs. 5(a) and 5(b), were measured simultaneously. Positions of the main layers of the laser are marked on the AFM image using the known locations of the layers with respect to the edge of the facet; see Figs. 1(c) and 1(d). If necessary, it is possible to directly reveal all the main layers of the heterostructure laser using standard AFM cantilevers with sharper tips, see e.g [22,23]. According to the measurements at the emitting facet, Fig. 5(c), the SNOM profile has three peaks located within the waveguide layer. Figure 5(c) also shows the calculated profile expected for the 2nd TE mode. In contrast to the model, the experimental profile is asymmetrical: the right peak is notably above the other two peaks.

The observed local near-field could result from mixing the 1st mode (odd mode with two extremes and zero electric field in the center of the waveguide) to the main 2nd mode. The contribution of the 0th mode (the only electric field extremum in the middle of the waveguide) to the near-field is excluded for four reasons: any linear combination of the 2nd and the 0th modes produces a symmetrical near-field; since the central peak is not the biggest, the 0th mode cannot be the main one; since the central peak is not the smallest, the 1st mode cannot be the main one; a simultaneous excitation of all three modes is unlikely.

In frame of the model with Eq. (1b), the ratio of the peak heights in Fig. 5(c), $S_L/S_R \cong 0.8, S_R/S_C \cong 1.4$, may be used to evaluate the contributions from the 1st and the 2nd modes to the local near-field. We take “1” and “ δ ” for the electric field amplitude of the 2nd mode, and, correspondingly, the 1st mode; the phase shift between the two modes is defined as φ . An arbitrary combination of these modes is given by the following values of the amplitudes:

$$A_L = -1 + \delta \times e^{i\varphi}; A_C = 1; A_R = -1 - \delta \times e^{i\varphi} \quad (2)$$

Taking into account $S_L : S_C : S_R = |A_L|^2 : |A_C|^2 : |A_R|^2$, the unknown variables in Eq. (2) are uniquely expressed in terms of the peak heights ratio in the measured SNOM signal: $\delta = \sqrt{0.5(S_L/S_C + S_R/S_C)} - 1$; $\cos(\varphi) = (S_R/S_C - S_L/S_C)/(4\delta)$. In particular, for the data in Figs. 5(a) and 5(b), we obtain: $\delta \cong 0.3; \varphi \cong 60^\circ$. Thus, locally, in the measured region, the near-field contains approximately 75% of the 2nd mode and 25% of the 1st one. It is worth noting that observed ratio and phase parameters do not strongly deviate from the parameters we used to reconcile calculated and measured data in Fig. 1(a): $\delta = 0.267; \varphi = 16^\circ$. The last parameters may characterize the near-field, averaged over the entire $100 \mu\text{m}$ -aperture of the emitting facet.

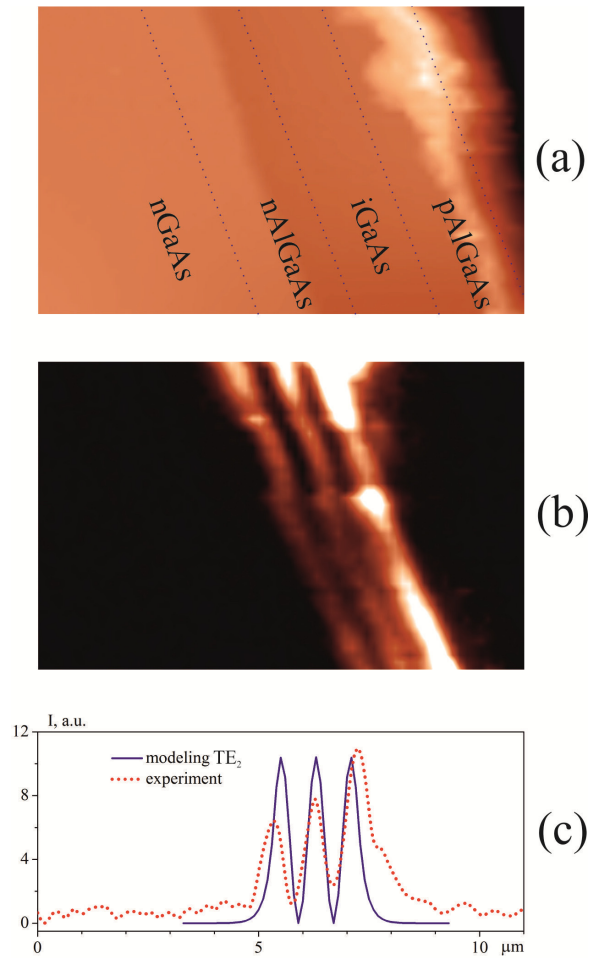


Fig. 5. SNOM study of the radiation distribution at the emitting facet of the active laser diode. A contact AFM image of the surface topography on emitting facet, (a). A SNOM XY image of the light distribution, (b). A typical X-profile of SNOM signal (red dotted line) and a model profile (blue solid line) for the near field expected for the 2nd TE mode, (c), see also Fig. 1(b).

The experimentally determined structure of the local near-field was used to simulate the model XZ image in Fig. 6(a). A signal for the modeling image was calculated by the Eq. (1b) with the following parameters: $A_L = -1 + 0.3 \times e^{ix\pi/3}$; $A_C = 1$; $A_R = -1 - 0.3 \times e^{ix\pi/3}$. A modeling takes also into account the angle $\alpha \cong 23^\circ$ between the ridges in Fig. 5(b) and the Y scanning direction: the distance between the measuring point, r , and the source, r_i , $|r - r_i| = \sqrt{(z - z_i)^2 + (x - x_i)^2 \times (\cos \alpha)^2}$; $i = L, C, R$.

The SNOM image of the laser radiation distribution in the same XZ plane is shown in Fig. 6(b). As in confocal microscopy, see Fig. 4(b), SNOM also reveals the light propagates along three directions (lobes). Additionally, at the distance of several wavelengths from the emitting facet, the right lobe is the brightest, while the central lobe becomes the weakest. This is in very good agreement with the far-field radiation divergence in Fig. 1(a), as well as with the simulation results in Fig. 6(a). The SNOM image, however, demonstrates extra details. At a distance from the emitting facet, the signal intensity varies with a period of about a half wavelength. Several oscillations of the signal are on the left and central lobes, the best way they are revealed on the right lobe. We explain such oscillations are caused by the light

interference in the cavity between the emitting facet and the probe over the surface. This is similar to the effect of antireflection coatings for optical instruments.

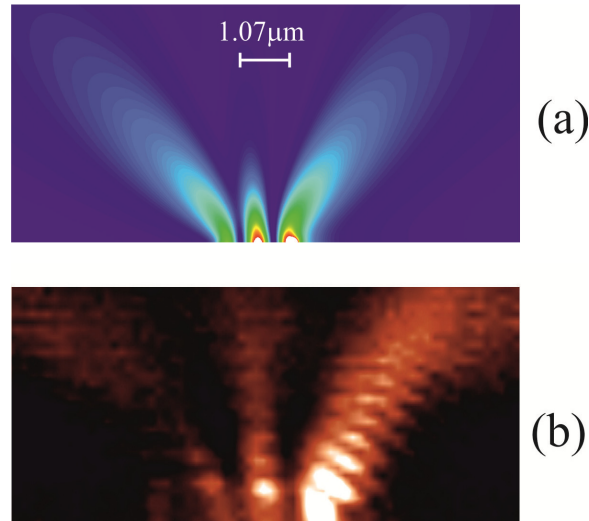


Fig. 6. SNOM study of the radiation distribution near the emitting facet of the active laser diode. A model XZ image, (a). A SNOM XZ image (integrated intensity of spectrum signal in the 1068-1079 nm range), (b).

3. Conclusions

The radiation distributions near the emitting facet of an operating high-power laser diode have been investigated by scanning confocal optical microscopy and SNOM. In the studied laser, the active region has been shifted from the waveguide center towards the p-emitter to provide the most favorable conditions for generation of the 2nd and 1st TE modes and to create a light source with a large angle of radiation divergence in the far-field. We show that measurements using a confocal microscope can give a distorted picture of the near-field radiation from such a laser, even when using an air lens with $NA = 0.9$. Accurate data on the near-field intensity at the emitting facet was obtained with sub-wavelength spatial resolution using the technique based on the integration of an optical spectrometer and SNOM with aperture cantilever. This technique, however, may perturb the distribution of light from the laser when the cantilever's probe is lifted above the radiating facet. Due to the light interference between the surfaces of the probe and the emitting facet, additional spatial oscillations of the signal in Z-direction may appear. This effect can be further minimized by sharpening the SNOM probe or by reducing reflectance of the metal coating by increasing its roughness.

The experimental images were compared with the images from the model signal, which was calculated as the time-average contribution of three damped sine waves. The sources of such waves located at the extrema of the electric field distribution of the 2nd TE mode corresponding to the solution of the wave equation for the dielectric waveguide laser. On the emitting facet, in the near-field, an asymmetric distribution of the radiation was revealed, which manifests the mixing of the odd and even (1st and 2nd) modes. Satisfactory agreement between the results of simulation and experiment was obtained. This made it possible to establish the configuration of the local near-field: the ratio of the electric field amplitudes of the 1st and the 2nd modes and the phase delay.

We believe the results of this study are important for the technology of semiconductor lasers with predetermined modal compositions.

Acknowledgments

The work was partially supported by FTP (SC N° 16.526.12.6017), RAS Presidium program N° 24, and by Government of Russian Federation (Grant 074-U01).